AIAA JOURNAL
Vol. 40, No. 11, November 2002

Two-Dimensional Simulations of Wake Vortex Detection Using Radio Acoustic Sounding Systems

Said Boluriaan* and Philip J. Morris†
Pennsylvania State University, University Park, Pennsylvania 16802

A parallel code is developed to simulate numerically wake vortex detection using a radio acoustic sounding system (RASS). The code is written in FORTRAN 90 with the message passing interface for parallel implementation. The numerical simulation solves simultaneously the linearized Euler equations for a nonuniform mean flow and the Maxwell equations for a nonhomogeneous medium. The radar transmitter and receiver antennas are modeled using an array of point sources and a beam-forming technique, respectively. Many features of the RASS are explored using the numerical simulation. First, a uniform mean flow is considered, and the RASS simulation is performed for two different types of incident acoustic field: a short single-frequency acoustic pulse and a continuous broadband acoustic source. Both monostatic and bistatic configurations are examined, and their results are compared. Taylor and Oseen vortex velocity profiles are used as sample models, and their mean flowfields are reconstructed from the backscattered electromagnetic signal using the Abel transform. The effect of radar beam width is also considered, as are the issues of nonaxisymmetric and interacting vortices.

I. Introduction

THE capacity of airports is constrained severely by the air traffic control system's consideration of aircraft wake vortices. The present Instrument Flight Rules (IFR) restrictions are based on aircraft weight. The "3–4–5–6 rule" sets the separation distances of aircraft by categories from small, less than 41,000 lb (18,600 kg), to heavy, greater than 255,000 lb (116,000 kg). These separations are viewed as very conservative. However, because there remains significant uncertainty about wake vortex behavior under different atmospheric conditions, there are considerable technological barriers to improvements in terminal area productivity.

In an attempt to enhance airport capacity, an aircraft vortex spacing system (AVOSS) has been under development at NASA Langley Research Center. The AVOSS will provide the means to allow air traffic control to reduce spacing safely in instrument operations when the appropriate weather conditions exist. A key element in AVOSS is the development of a real-time reliable wake vortex detection system (WVDS).

A radio acoustic sounding system (RASS) is a promising candidate for a WVDS. The basic concept of RASS is based on the tracking of sound waves with radar. When acoustic waves are transmitted, they produce pressure perturbations, which lead to fluctuations in the atmospheric permittivity. An incident electromagnetic field is then scattered due to the permittivity variations and generates an echo that can be detected by a receiver antenna. The spectrum of this echo shows a Doppler shift proportional to the local speed of sound. However, the backscattered signals are so weak that no measurable signal would be received unless the Bragg condition is satisfied. The Bragg condition is a relationship between the incident electromagnetic and acoustic wavelengths that ensures a constructive interference between the two waves. The Bragg condition may be written as

$$\lambda_e = 2\lambda_a \sin\alpha \tag{1}$$

where λ_a and λ_e are the incident acoustic and electromagnetic wavelengths, respectively, and α is the incident radar beam angle (shown later).

Received 23 January 2001; revision received 11 April 2002; accepted for publication 30 May 2002. Copyright © 2002 by Said Boluriaan and Philip J. Morris. Published by the American Institute of Aeronautics and Astronautics, Inc., with permission. Copies of this paper may be made for personal or internal use, on condition that the copier pay the $10.00 per-copy fee to the Copyright Clearance Center, Inc., 222 Rosewood Drive, Danvers, MA 01923; include the code 0001-1452/02 $10.00 in correspondence with the CCC.

*Postdoctoral Research Associate, Department of Aerospace Engineering. Member AIAA.
†Boeing/A. D. Welliver Professor, Department of Aerospace Engineering. Fellow AIAA.

The application of RASS as a ground-based remote sensing technique goes back more than 30 years, when Smith[1] and Fetter[2] used a radio-acoustic detection system to measure wind velocity. They chose a 10-GHz radar and a 22-kHz acoustic source to meet the Bragg condition. This choice was based largely on the ready availability of microwave equipment and techniques in the X band and had the definite advantage of placing the frequency of the high-intensity acoustic energy above the normal hearing range. The accuracy of their device was poor, and the range was limited to 90 m. In 1972, Marshall et al.[3] realized that Smith[1] and Fetter[2] chose a high-power acoustic source with a very short wavelength, which caused the acoustic waves change into the shock waves and dissipate rapidly. Therefore, Marshall et al.[3] used a 36.8-MHz radar and an 85-Hz acoustic source and were able to detect atmospheric temperature up to 1.5 km within a reasonable accuracy.

Measurements of the temperature profile using RASS were first reported by North et al.[4] The maximum range of their system varied from about 400 m to nearly 3 km. They found that two atmospheric phenomena reduced the strength of the returned signal: The turbulence disturbed the shape of the sound wave and the crosswind displaced the acoustic pulse downwind and out of the radar sight. Although increasing the acoustic wavelength could reduce the effect of turbulence, the crosswind effect remained a challenging problem.

In recent years the RASS technique has been applied to temperature and wind velocity measurement over a wide range of altitudes, from the troposphere[5–7] to the lower stratosphere,[8] and also to measurements of heat flux in the atmospheric boundary layer.[9] The concept of a RASS has also been applied to measure atmospheric parameters such as wind velocity and the turbulence field. The effect of turbulence on RASS measurements and measurements of atmospheric turbulence itself using a RASS are described by Tatarski,[10] Nalbandyan,[11] Kon,[12,13] and Bhatnagar and Peterson,[14] among many other researchers. In 1995, a series of measurements were performed in Norway under the Environmental Surveillance Technology Programme.[15,16] The measurements show that, by using a sensitive system involving many rf frequencies, it is possible to determine many of the parameters that characterize the atmosphere. These parameters include three-dimensional wind velocity, turbulence and vortex activity, wind shear and down draft, and atmospheric stability.

Recently, RASS has received particular attention as a potential tool to detect vortices behind aircraft in the vicinity of airports.[17] Here, the concept is similar to wind measurements; in the presence of an aircraft wake vortex, the effective speed of acoustic propagation changes, and this provides an additional Doppler shift in the spectrum. As is shown in this paper, the vortex velocity field

may be obtained based on a spectral analysis of the backscattered electromagnetic signal.

All of these experiments show the feasibility and applicability of RASS as a remote sensing tool for wake vortices and other atmospheric parameter measurements. However, experiments usually suffer from the mixing and interaction of different parameters and factors. A study under the fully controlled environment of a numerical simulation can help to understand the contributions of the different factors.

In a previous study by the authors,[18] a two-dimensional Euler, one-dimensional Maxwell code was developed to simulate wake vortex detection using RASS. Many features of the RASS were captured successfully in that study. The major contribution of the present paper is the provision of a full two-dimensional numerical simulation for the RASS parametric study. This is achieved not only by a direct computation of the acoustic and scattered electromagnetic fields, but also by a realistic modeling of the transmitter and receiver antennas. Such a modeling makes it possible to study the effects of beam width, the antennas' locations, and the RASS in a bistatic configuration. The present paper also considers the case in which the RASS uses continuous incident acoustic and electromagnetic fields, which is an alternative to the traditional pulse radar.

In the next section, the basic equations for electromagnetic and acoustic wave propagation as well as the relationship between the pressure perturbations and the permittivity fluctuations are presented. Then the method used to model the transmitter and receiver antennas is described. This is followed by a description of the Abel transform and the vortex models that are used. The numerical implementation is then given, which is followed by some example results and conclusions.

II. Analysis

The basic equations for a RASS simulation are described in this section. These equations include the Maxwell and linearized Euler equations and an auxiliary equation to relate the permittivity fluctuations and pressure perturbations.

A. Equations for Electromagnetic Wave Propagation and Scattering

The propagation and scattering of electromagnetic waves satisfy the Maxwell equations. For the RASS application, the Maxwell equations for a nonconductive medium without charge are considered. Then the electric and magnetic field intensity vectors are split into incident and scattered fields. The incident field may be specified analytically. Furthermore, the magnetic field intensity vector may be eliminated in favor of the electric field. Then, the differential equation that governs the scattered electric field becomes[18]

$$\nabla(\nabla\cdot\boldsymbol{E}_s)-\nabla^2\boldsymbol{E}_s+\frac{1}{c^2}\frac{\partial^2\boldsymbol{E}_s}{\partial t^2}=-\mu\frac{\partial^2}{\partial t^2}(\Delta\epsilon\boldsymbol{E}_i) \tag{2}$$

where $c=(\mu_0\epsilon_0)^{-1/2}$ is the speed of light and $\Delta\epsilon=\epsilon-\epsilon_0$ is the permittivity perturbation. The incident and scattered electromagnetic field are denoted by E_i and E_s, respectively. Equation (2) neglects multiple scattering, and it is assumed that the permeability of the medium, μ, is constant throughout the scattered field.

B. Equations for Acoustic Wave Propagation

The propagation and scattering of acoustic waves are described by the linearized Euler equations. In the RASS simulation the acoustic source is located far from the vortex center. Therefore, the mean flow velocity in the vicinity of the source is neglected. This makes it possible to ignore the effect of the source on the right-hand side of the momentum equations and also allows the replacement of the right-hand side of the energy equation by c_{a0}^2S, where c_{a0} is the free-space sound speed. The governing differential equations for a two-dimensional flow with nonuniform mean flow quantities then become

$$\frac{\partial\rho'}{\partial t}+\rho'\left(\frac{\partial\bar{u}}{\partial x}+\frac{\partial\bar{v}}{\partial y}\right)+\bar{\rho}\left(\frac{\partial u'}{\partial x}+\frac{\partial v'}{\partial y}\right)+u'\frac{\partial\bar{\rho}}{\partial x}+v'\frac{\partial\bar{\rho}}{\partial y}+\bar{u}\frac{\partial\rho'}{\partial x}+\bar{v}\frac{\partial\rho'}{\partial y}=S$$

$$\frac{\partial u'}{\partial t}+\bar{u}\frac{\partial u'}{\partial x}+\bar{v}\frac{\partial u'}{\partial y}+u'\frac{\partial\bar{u}}{\partial x}+v'\frac{\partial\bar{u}}{\partial y}+\frac{\rho'}{\bar{\rho}}\left(\bar{u}\frac{\partial\bar{u}}{\partial x}+\bar{v}\frac{\partial\bar{u}}{\partial y}\right)+\frac{1}{\bar{\rho}}\frac{\partial p'}{\partial x}=0$$

$$\frac{\partial v'}{\partial t}+\bar{u}\frac{\partial v'}{\partial x}+\bar{v}\frac{\partial v'}{\partial y}+u'\frac{\partial\bar{v}}{\partial x}+v'\frac{\partial\bar{v}}{\partial y}+\frac{\rho'}{\bar{\rho}}\left(\bar{u}\frac{\partial\bar{v}}{\partial x}+\bar{v}\frac{\partial\bar{v}}{\partial y}\right)+\frac{1}{\bar{\rho}}\frac{\partial p'}{\partial y}=0$$

$$\frac{\partial p'}{\partial t}+\gamma p'\left(\frac{\partial\bar{u}}{\partial x}+\frac{\partial\bar{v}}{\partial y}\right)+\gamma\bar{p}\left(\frac{\partial u'}{\partial x}+\frac{\partial v'}{\partial y}\right)+u'\frac{\partial\bar{p}}{\partial x}+v'\frac{\partial\bar{p}}{\partial y}+\bar{u}\frac{\partial p'}{\partial x}+\bar{v}\frac{\partial p'}{\partial y}=c_{a0}^2S \tag{3}$$

where ρ, p, and t are density, pressure, and time, respectively. In Eq. (3), u and v represent the Cartesian velocity components in the x and y directions, respectively. An overbar indicates a mean quantity and primes denote fluctuations about the mean. S denotes the acoustic source, which in the present study is taken to be

$$S(x,y,t)=\xi\Phi(t)\exp\left\{-\sigma_s\left[(x-x_0)^2+(y-y_0)^2\right]\right\}\sin\omega_a t \tag{4}$$

where

$$\Phi(t)=\exp\left[-\sigma_t(t-t_0)^2\right]$$

and t_0 is the pulse delay time. Here, ξ, σ_s, and σ_t are parameters that control the amplitude and the width of the pulse in space and time, respectively. The acoustic frequency is ω_a, and the source is located at (x_0, y_0).

C. Permittivity Variations in Atmosphere

The link between the Maxwell and Euler equations is the relationship between the pressure perturbation and the permittivity fluctuations. This relationship for a dry atmosphere with a uniform mean temperature equal to 300 K can be written as[18]

$$\Delta\epsilon=\epsilon-\epsilon_0=5.1715\times10^{-9}p' \tag{5}$$

where p' is in pascal. The effect of mean temperature variation and humidity can also be taken into account.

D. Modeling of the Transmitter and Receiver Antennas

The transmitter and receiver antennas are major components of a RASS. The transmitter antenna provides the electromagnetic incident field and it should generate a narrow beam in the desired direction with minimum sidelobes. The backscattered electromagnetic signals are collected in a receiver. A receiver antenna has to be able to focus in any given direction. A poor design of transmitter and/or receiver antennas results in a low signal-to-noise ratio and the reception of undesired or false signals.

1. Transmitter Antenna

The transmitter antenna is modeled using an array of point sources. Consider N identical isotropic point sources of equal amplitude and spacing. Then the far-field radiation pattern can be written as[19]

$$\mathcal{E}_p=E_0\{1+e^{i\Psi}+e^{i2\Psi}+\cdots+\exp[i(N-1)\Psi]\}$$

$$=E_0\sum_{n=1}^{N}\exp[i(n-1)\Psi] \tag{6}$$

where $\Psi=k_ed\cos\phi+\delta$ and d is the spacing between sources. Here, δ is the progressive phase difference of adjacent sources, that is, source 2 with respect to 1, 3 with respect to 2, etc. Also, k_e is the point source wave number and ϕ is the azimuthal angle measured with respect to the array.

There are two popular configurations based on the value chosen for the phase difference δ: broadside and end fire. In the broadside configuration, $\delta=0$, and the direction of maximum radiation

is normal to the source array. For a long array consisting of N point sources, the half-power beam width (HPBW) in radians in this configuration may be estimated by[19]

$$\text{HPBW} \simeq \lambda_e/Nd \tag{7}$$

where λ_e is the incident electromagnetic wavelength.

For an end-fire array, the direction of maximum radiation is in the direction of the source array. To achieve this configuration, the progressive phase difference between sources δ should be $-k_e d$. Then the HPBW may be approximated by[19]

$$\text{HPBW} \simeq \tfrac{4}{3}\sqrt{2\lambda_e/Nd} \tag{8}$$

For a given number of point sources, the broadside array provides a smaller beam width in the two-dimensional case.

A "binomial array" may also be used to eliminate the radiation pattern sidelobes. In this case, the point sources in Eq. (6) have amplitudes proportional to the coefficients of a binomial series. An elegant aspect of a binomial array is that the radiation pattern of this array has a very simple mathematical description:

$$\mathcal{E}_p = \cos^{N-1}\left(\tfrac{1}{2}k_e d\cos\phi\right) \tag{9}$$

The drawback of using binomial arrays is that, for a given number of sources, the HPBW of a binomial array is considerably wider than a broadside array.

2. Receiver Antenna

The main purpose of using a receiving antenna is to collect and enhance signals that propagate toward the receiver from a certain direction. This may be achieved by using a receiver array and a beamforming technique. A receiver array consists of discrete receivers called array elements. The signals received in individual elements are combined together with different phase delay. The phase delay for each element is chosen such that the array focuses or steers in a certain direction. Focusing the array means the phase delay is selected such that signals that come from a particular point are in phase for all of the elements. Steering the array means selecting phase delays so that all signals that come from a certain direction are in phase for all elements.

The theory behind receiver arrays is similar to that for the transmitter arrays described in the preceding sections. For example, in a linear array with equally spaced elements, if all signals are summed in phase, an array pattern similar to the broadside array is obtained. In other words, this array enhances all signals that come from the direction normal to the elements' axis. An end-fire type directivity may be obtained by adding up the output of each element with a phase delay that corresponds to the element spacing and the wave speed.

Similar to the transmitter array, a broadside receiver has a smaller aperture angle compared to the end-fire receiver. The aperture angle may be reduced by increasing the number of elements. The concept of a binomial array may also be used to eliminate sidelobes. For a binomial receiver, the signals collected at each element are summed with a weighting function proportional to the binomial series coefficients.

E. Abel Transform

An analysis of the electromagnetic scattered signal can only reveal the component of the wake vortex velocity profile in the direction of the incident radar beam, that is, along the dash–dotted line in Fig. 1. However, it is often desirable to obtain the radial variation of the vortex velocity field, $V(r)$. The Abel transform and its inverse provide the necessary mathematical tool for such a task. Assume that the integral of an axisymmetric function, $V(r)$, is known along a line from $-Y(x)$ to $Y(x)$ for any given x (Fig. 1). Then, it is possible to determine the vortex radial velocity field $V(r)$ using the inverse Abel transform (see Ref. 18):

$$V(r) = \frac{1}{\pi r}\left[\frac{RQ(R)}{\sqrt{R^2-r^2}} - \int_r^R \frac{xQ'(x)\,\mathrm{d}x}{\sqrt{x^2-r^2}}\right] \tag{10}$$

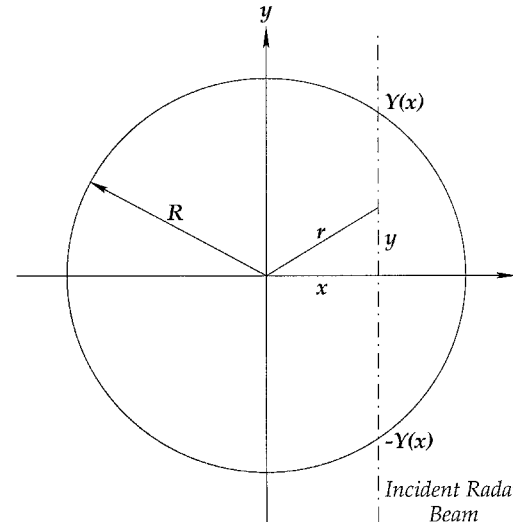

Fig. 1 Application of the Abel transform to wake vortex velocity.

where

$$Q(x) = \int_{-Y(x)}^{Y(x)} \frac{x}{r}V(r)\,\mathrm{d}y, \qquad 0 \le x \le R \tag{11}$$

The integrand of the preceding integral is the vortex velocity field in the direction of the radar beam and may be obtained once the backscattered signal is analyzed.

In practice, $Q(x)$ is available as a discrete data set, and a numerical transform technique has to be used. Here, the numerical method proposed by Nestor and Olsen[20] has been applied. This method has been slightly modified to best fit the RASS application.

F. Vortex Models

Taylor and Oseen vortices are considered as models for an aircraft wake vortex in this paper. As noted by de Neufville,[21] the vorticity distribution of any incompressible unsteady vortex may be written in terms of a linear combination of various vortex modes. Both Oseen and Taylor vortices correspond to the two leading modes in the general solution.

The azimuthal velocity distribution, $v_\theta(r)$, of a Taylor vortex may be written as[22]

$$v_\theta/V_c = (r/r_c)\exp\left\{\tfrac{1}{2}\left[1-(r/r_c)^2\right]\right\} \tag{12}$$

where r_c and V_c are the core radius and velocity, respectively.

An Oseen vortex is described by (see Ref. 23)

$$v_\theta/V_c = \alpha(r_c/r)\left\{1-\exp\left[-\beta(r/r_c)^2\right]\right\} \tag{13}$$

where $\alpha = 1.397950$ and $\beta = 1.256435$ are chosen such that the maximum velocity occurs at the core radius.

III. Numerical Implementation

The numerical simulation of RASS consists of the solution of two sets of equations: the linearized Euler equations and the Maxwell equations. In the first, the total acoustic field is determined numerically. The linearized Euler equations are discretized using a fourth-order dispersion-relation-preserving algorithm[24] in space and a fourth-order Runge–Kutta scheme in time.

Once the acoustic field is reconstructed at any instant, the pressure perturbations may be used to determine the permittivity perturbation $\Delta\epsilon$ throughout the solution domain using Eq. (5). The incident electromagnetic field is specified analytically by the transmitter antenna model. Therefore, the right-hand side of Eq. (2), the source term for the Maxwell equation, is determined. Then, the electromagnetic scattering problem is solved using a second-order central difference scheme both in space and time. The details of the Maxwell solver scheme, as well as its numerical stability characteristics, may be found in Ref. 25. No artificial dissipation is used in the Maxwell solver. Because the speeds of sound and light are so different, the

medium, including the vortex and acoustic field, appear frozen in time relative to the electromagnetic wave. Thus, the electromagnetic wave is assumed to be propagating through a stationary, nonuniform medium. In fact, a few hundred time steps in the Maxwell solver take place between each time step of the Euler calculation.

A radiation boundary condition is used for both the acoustic and electromagnetic scattering. For the Euler calculation, the radiation boundary condition developed by Tam and Webb[24] is used. For the Maxwell calculation, the nonreflecting boundary condition described by Bayliss and Turkel[26] is applied.

IV. Results

In this section, the results of a full two-dimensional simulation are presented. In all simulations the Bragg condition is completely or nearly satisfied to enhance the scattered field and maximize the signal-to-noise ratio. An explicit scheme with a reduced, fictitious speed of light equal to 3×10^5 m/s is used throughout this section. The results of a previous study by authors[18] have shown the validity of this approach. The use of an explicit scheme facilitates parallelization, which is necessary for the present study. The simulations are performed on a uniform grid, and 12 grid points per acoustic wavelength are used. A typical simulation takes approximately 340 h to complete. This is the one-processor equivalent wall clock CPU time. Usually 16 processors are used for each case. A complete parallel performance analysis may be found in Ref. 25.

A. Model Problem for Uniform Mean Flow

To validate the two-dimensional RASS simulation, a uniform mean flow is considered first. For a uniform mean flow, the solution to the Euler equations may be specified analytically, and only the Maxwell equations need to be solved numerically. The mean flow velocity is taken to be 50.0 m/s in a direction away from the transmitter. Both monostatic and bistatic RASS configurations are explored.

1. Two-Dimensional Monostatic RASS Model

In this case, the frequencies of the incident electromagnetic and acoustic field are chosen to be 900 kHz and 2040 Hz, respectively. The Bragg condition is only met in the absence of the mean flow, and the simulation is performed slightly off the Bragg condition for the given mean flow velocity. A continuous electromagnetic incident field and an acoustic pulse are used. A broadside array of 161 isotropic point sources is used to generate an incident electromagnetic beam with HPBW equal to 0.7118 deg. Figure 2 shows the scattered electromagnetic field at different times. In Fig. 2, the transmitter antenna and acoustic source are located at $(0, -24\lambda_a)$ and the scattered electromagnetic field is sampled at $(0, -18\lambda_a)$. Notice that the amplitude of the scattered field in Figs. 2d is very small and is about 10 times less than Figs. 2a and 2c and 100 times less than Fig. 2b. The minute oscillations in Fig. 2d are due to some small numerical reflection at the boundaries. Extending the

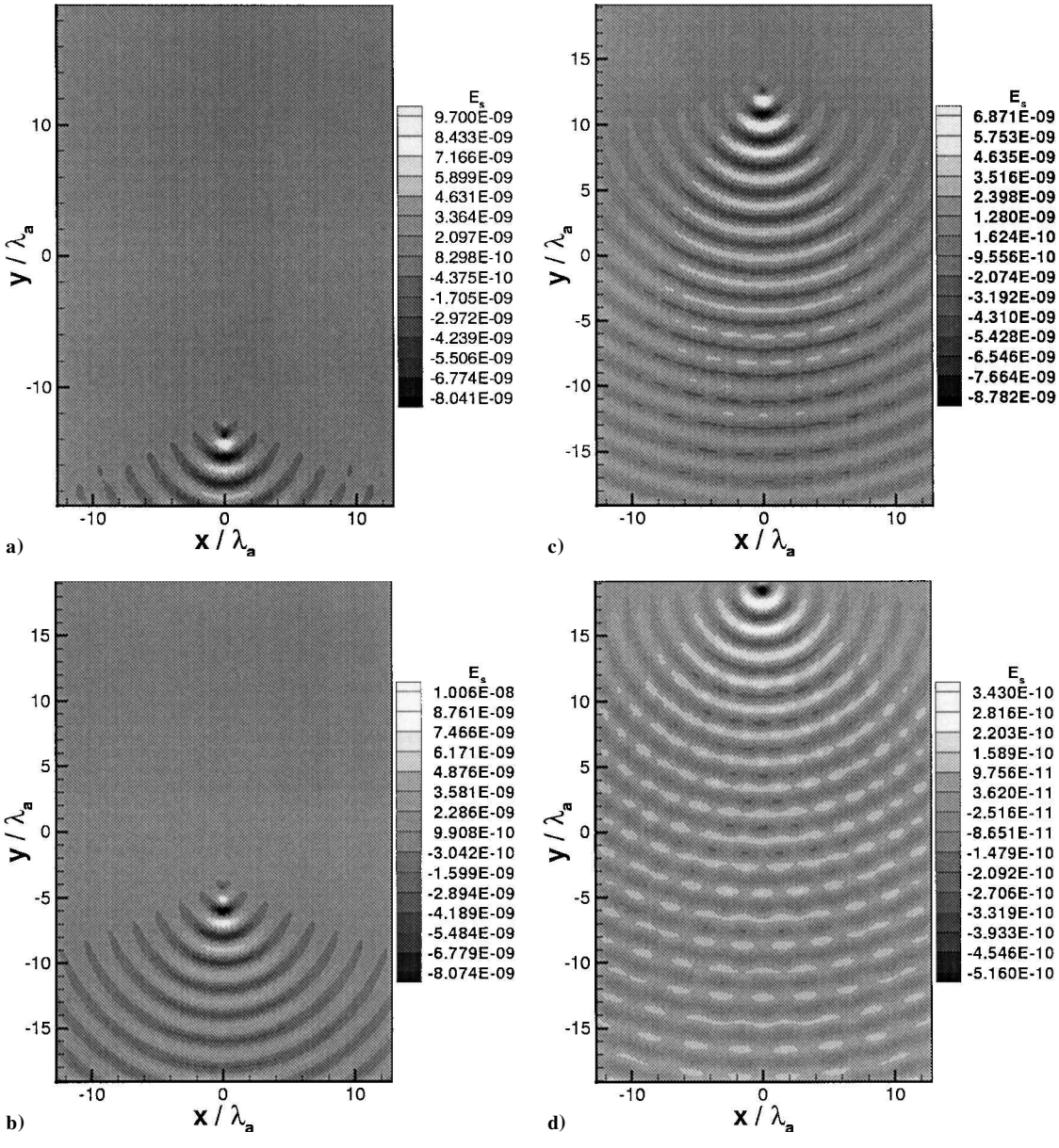

Fig. 2 Electromagnetic scattered field for uniform mean flow in monostatic configuration: a) $t = 0.003$ s, b) $t = 0.006$ s, c) $t = 0.012$ s, and d) $t = 0.015$ s.

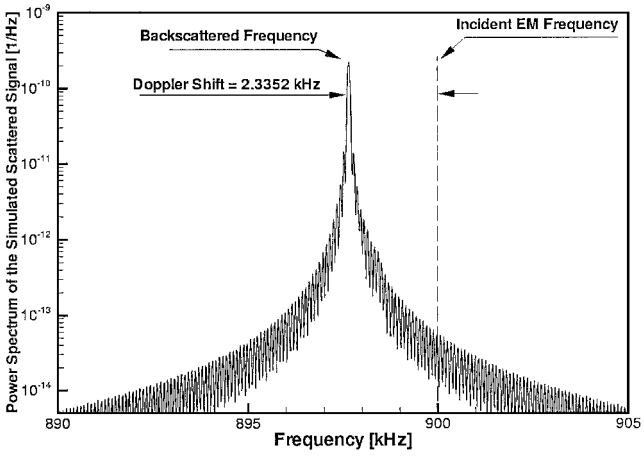

Fig. 3 Power spectrum of the simulated scattered signal in uniform mean flow.

computational domain was observed to not change the significant part of the backscattered signal.

Figure 2 may be used to explain some fundamental concepts in the RASS. An acoustic pulse is a region of density variations. A density variation gives rise to a variation in refraction index or permittivity. As the incident electromagnetic waves pass through this region of variable permittivity, they are scattered. The frequency of the scattered electromagnetic wave is equal to the incident electromagnetic frequency for an observer moving with the acoustic pulse. For a stationary observer, however, the acoustic pulse acts like a moving source. This source moves with a velocity equal to the local speed of propagation, that is, the vector summation of the local sound speed and mean flow velocity. A stationary observer then receives backscattered electromagnetic signals that include a Doppler shift proportional to the local pulse speed.

Figure 3 shows the frequency spectrum of the simulated scattered signal. To perform a Fourier transform, 450,000 samples at a sampling frequency equal to 41 MHz are taken and zero padded to $2^{21} = 2{,}097{,}152$ samples. The spurious sidelobes in Fig. 3 are the result of this zero padding. Although a relatively high zero padding is used, the main lobe level is still more than one decade (10 dB) higher than the largest sidelobes.

The Doppler shift in the backscattered field, shown in Fig. 3, is related to the local propagation speed of the acoustic waves in the transmitter direction, C_a, by[18]

$$f_d = (2f_e/c)C_a \tag{14}$$

where f_d and f_e are the Doppler shifted frequency and radar wave frequency, respectively, both in hertz, and c is the propagation speed of the electromagnetic waves. C_a consists of two components: the local sound speed and local mean flow velocity. The Doppler shift given by the spectrum in Fig. 3 equals 2335.2 Hz, of which 2040 Hz is due to the local sound speed and 295.2 Hz is due to the mean flow contribution. The frequency shift of 295.2 Hz corresponds to 49.207 m/s for the given conditions. The frequency resolution in Fig. 3 is 19.5493 Hz, which corresponds to 3.2582 m/s. Thus, the difference between the velocity calculated from the Doppler shift and the exact value of the mean flow velocity is well within the resolution of the Fourier transform.

2. Continuous Broadband Acoustic Source

In this case, a numerical experiment is performed to investigate the case of a continuous incident acoustic field. The acoustic source continuously generates white noise within a frequency band centered on $2c_{a0}/\lambda_e$, where c_{a0} and λ_e are the nominal speed of sound and electromagnetic wavelength, respectively. In this particular simulation, the incident electromagnetic frequency and the nominal speed of sound are chosen to be 900 kHz and 340 m/s, respectively. An explicit scheme with a fictitious speed of light equal to 3×10^5 m/s is used. Thus, the incident acoustic frequency band is centered at 2040 Hz. The permittivity perturbation then may be modeled as the superposition of sinusoids with different frequencies

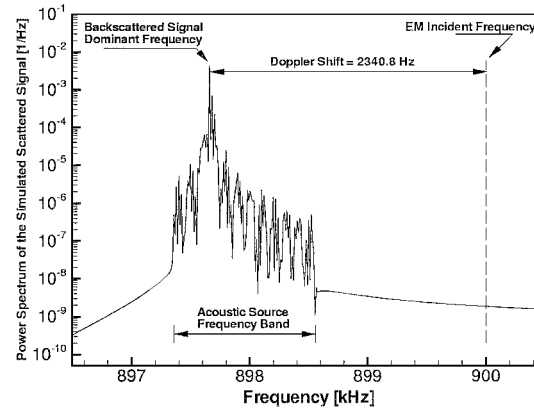

Fig. 4 Power spectrum of the simulated scattered signal in uniform mean flow for continuous incident acoustic field.

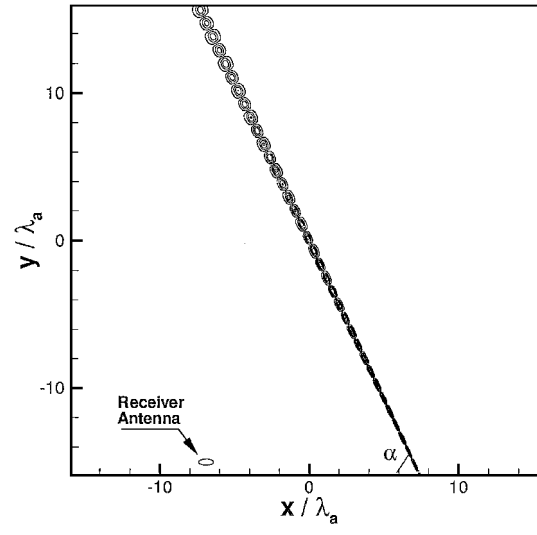

Fig. 5 Typical setup for a bistatic configuration; schematic of the incident electromagnetic waves and the location of the receiver antenna. Acoustic source (not shown) is at $(0, -20\lambda_a)$.

but the same amplitude and phase:

$$\Delta\epsilon = \sum_{n=-N}^{N} \Delta\epsilon_0 \cos[2\pi(f_{a0} + n\Delta f)t - k_a x] \tag{15}$$

where f_{a0} is the band center frequency in hertz, Δf is the frequency increment, and k_a is the acoustic wave number. In the numerical simulation presented here, Δf and N are taken to be 20 Hz and 30, respectively. Therefore, Eq. (15) provides a frequency band equal to 2040 ± 600 Hz, with a frequency increment equal to 20 Hz.

Figure 4 shows the power spectrum of the scattered signal. The incident electromagnetic frequency and the frequency band of the acoustic source are also shown. The frequency resolution in this plot is 10.786 Hz, which corresponds to 1.798 m/s. A Fourier transform is performed on $2^{21} = 2{,}097{,}152$ samples with no zero padding to avoid any spurious sidelobes. It can be seen that from all incident acoustic frequencies, one has the highest spectrum level. This is the frequency at which the Bragg condition is met. The incident electromagnetic wavelength is $\frac{1}{3}$ m for the given conditions. Thus, the Bragg matched acoustic wavelength is $\frac{1}{6}$ m. The Bragg matched acoustic frequency from the spectrum is 2340.8 Hz. When the acoustic frequency and wavelength are known, the local speed of propagation may be determined to be 390.135 m/s, of which 340 m/s is due to the local sound speed and 50.135 m/s is due to the mean flow velocity. The accuracy of this measured velocity is within the power spectrum resolution.

3. Two-Dimensional Bistatic RASS Model

Figure 5 shows a typical bistatic configuration. In Fig. 5 the acoustic source is located at $(0, -20\lambda_a)$. A narrow beam acoustic

pulse is used. The electromagnetic transmitter antenna is located at $(9\lambda_a, -20\lambda_a)$. A binomial array with 10,000 isotropic sources is employed to generate a narrow incident electromagnetic beam. The incident beam is also shown in Fig. 5. In this particular example the incident electromagnetic beam makes an angle of 65 deg with the x axis. The scattered electromagnetic field is sampled at $(-15\lambda_a, -7\lambda_a)$.

The mean flow velocity is chosen to be 50 m/s in the y direction. The incident electromagnetic and acoustic frequency are taken to be 900 kHz and 2052.8 Hz, respectively. Recall the Bragg condition in the bistatic case [Eq. (1)]:

$$\lambda_e = 2\lambda_a \sin\alpha$$

where α is as shown in Fig. 5. The Bragg condition is met for a mean flow velocity equal to 37.5 m/s for the given frequencies. Therefore, the simulation is performed slightly off the Bragg condition.

Figure 6 shows the electromagnetic scattered field at the moment when the acoustic pulse is about to cross the incident electromagnetic beam. Note the change in directivity of the scattered field in Fig. 6 compared to the monostatic case shown in Fig. 2.

Figure 7 shows a typical backscattered electromagnetic signal at the receiver antenna in the bistatic system. The acoustic pulse passes the incident electromagnetic beam for a short period of time. This is the only time at which a detectable signal is received by the receiver antenna. This is clearly seen in Fig. 7.

Figure 8 shows the frequency spectrum of the simulated scattered signal in the bistatic case. For this case, 100,000 samples are taken and are zero padded to $2^{19} = 524{,}288$. The main lobe in Fig. 8 is about 3 decades (30 dB) higher than the maximum sidelobes. The frequency resolution is 78.2461 Hz, which corresponds to 14.3892 m/s. The relationship between the Doppler shift and the mean flow velocity in a bistatic system is given by

$$\omega_d = 2k_e c_a \sin\alpha \tag{16}$$

where ω_d is the Doppler shift in radians per second, k_e is the electromagnetic wave number, c_a is the local speed of propagation, and α is the incident beam angle as shown in Fig. 5.

The Doppler shift given by the spectrum equals 2126.1 Hz, which corresponds to a velocity of 390.977 m/s, of which 340.0 m/s is the contribution of the sound speed and 50.977 m/s is due to the mean flow velocity. Note that the mean flow velocity is determined from the frequency spectrum with very good accuracy. However, it is found that a bistatic system is more sensitive to the Bragg condition compared to a monostatic system. If a bistatic RASS operates far from the Bragg condition, the accuracy of the velocity measurements drops dramatically.

To demonstrate this effect, a mean flow velocity equal to 50 m/s and an incident electromagnetic frequency equal to 900 kHz are considered. The numerical simulation is conducted for various values of incident electromagnetic beam angle α. For a given value of α, three different incident acoustic frequencies are examined. These frequencies are tuned for a mean flow velocity equal to 0, 25, and 37.5 m/s. The frequency resolution for this calculation is 78.246 Hz, which corresponds approximately to 14 m/s. This means that all measurements within a margin of 50 ± 7 m/s are acceptable. It can be seen from Fig. 9 that, when the incident acoustic frequency is tuned to 37.5 m/s for a mean flow velocity of 50 m/s, the RASS

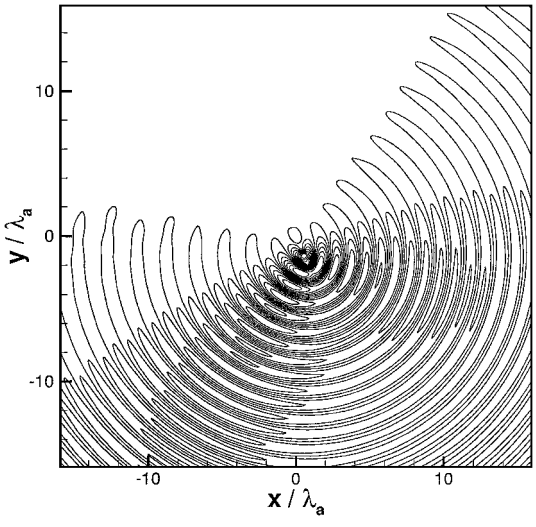

Fig. 6 Scattered electromagnetic field in the bistatic simulation.

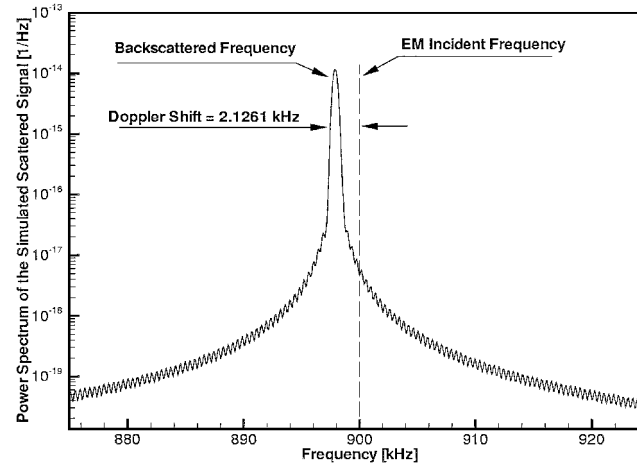

Fig. 8 Power spectrum of the simulated scattered signal in uniform mean flow and for a bistatic system.

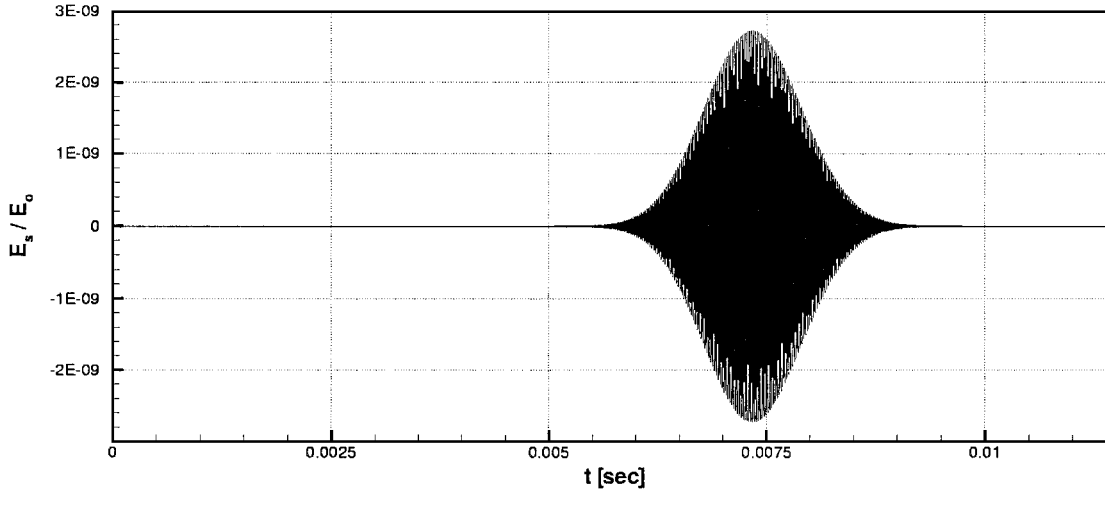

Fig. 7 Typical backscattered electromagnetic signal received in a bistatic system.

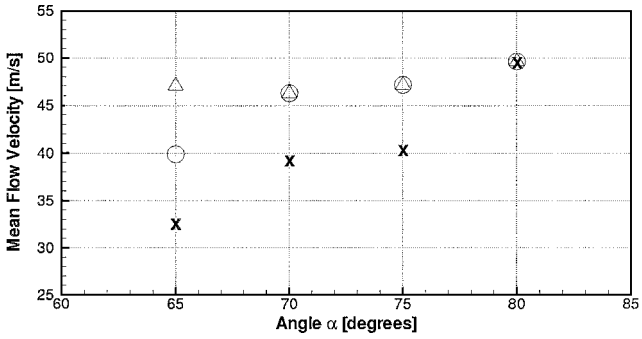

Fig. 9 Effect of the Bragg condition on the bistatic RASS measurements: uniform mean flow velocity is 50 m/s and the Bragg condition is matched for ×, 0 m/s; ○, 25 m/s; and △, 37.5 m/s.

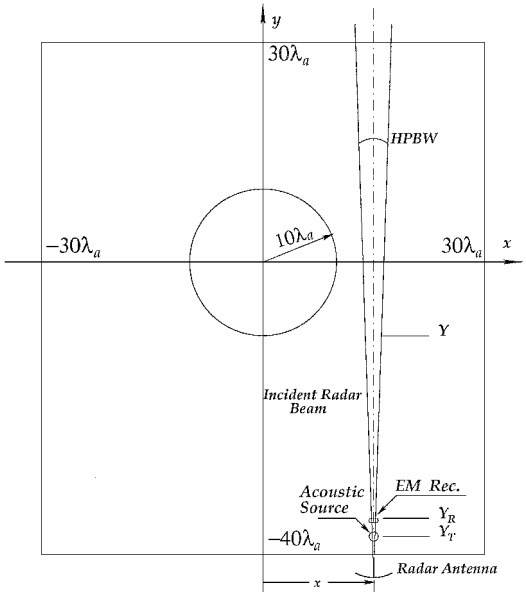

Fig. 10 Computational domain.

measurements are within the acceptable margin for all shown values of α. However, for the cases tuned to 25 and 0 m/s, the accuracy decreases for small angles α. It is also noticeable that, as α approaches 90 deg, that is, when system becomes close to a monostatic configuration, the RASS measurements are insensitive to the Bragg condition. In practice, however, a RASS device has to operate close to the Bragg condition to provide a sufficiently high signal-to-noise ratio.

B. Two-Dimensional Numerical Simulation

In the two-dimensional, direct numerical simulation both the Euler and Maxwell equations are solved simultaneously. The computational domain is shown in Fig. 10. An array of isotropic point sources is used to simulate the transmitter antenna and generate the incident electromagnetic field. The incident beam direction and width may be specified by the user. The incident acoustic field is generated by an acoustic source located at $y = -35\lambda_a$ and different x locations. This acoustic source is an omnidirectional monopole. To generate an incident acoustic pulse, the acoustic source is only turned on for a short period of time, sufficient to generate a pulse length equal to three acoustic wavelengths.

As the acoustic pulse travels through the computational domain, its wave front is modified due to the presence of the vortex. Figure 11 shows the incident acoustic pulse at different times for a Taylor vortex. The associated vortex core is also shown in Fig. 11. The vortex core radius is $10\lambda_a$. Slight reflections from the lower boundary of the computational domain are observed. This is because the acoustic source is located very close to the boundary and the angle of incidence is very small.

The electromagnetic and acoustic frequency in this case are chosen to be 900 kHz and 2040 Hz, respectively. Both Oseen and Taylor vortices have been considered as the aircraft wake vortex

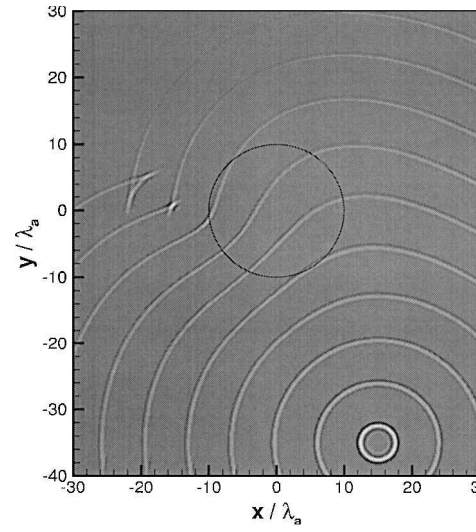

Fig. 11 Incident acoustic field at different times for a Taylor vortex; pulses from bottom to top correspond to $t = 20(2n-1)/\omega_a$ s, $n = 1, 2, 3, \ldots, 10$, respectively.

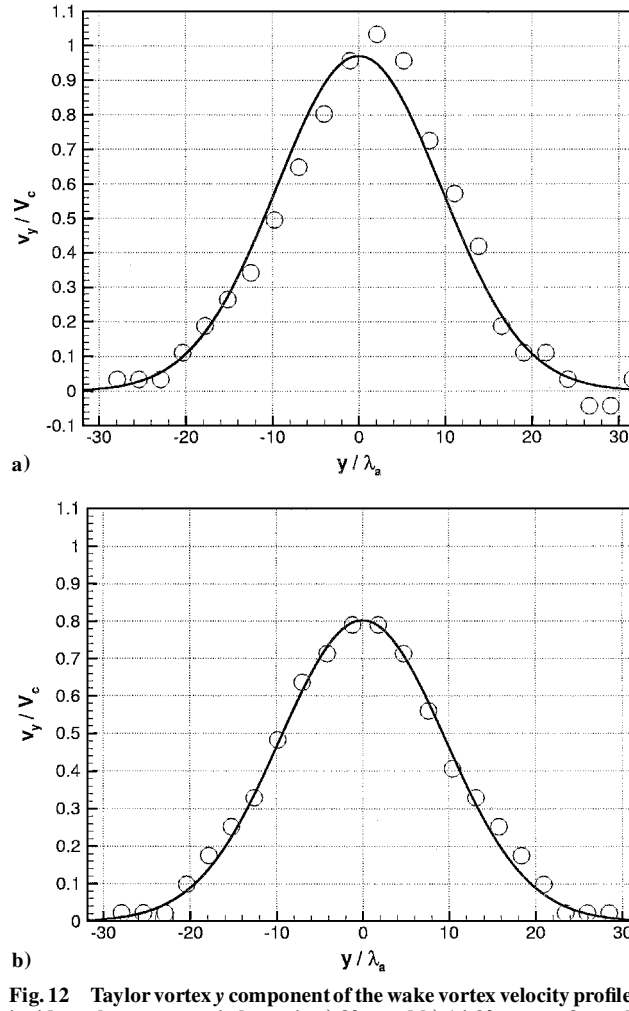

Fig. 12 Taylor vortex y component of the wake vortex velocity profiles: incident electromagnetic beam is a) $8\lambda_a$ and b) $14.3\lambda_a$ away from the vortex center in the x direction.

models. The core velocity V_c is taken to be 85 m/s for both of the vortices.

Figures 12 and 13 show the calculated vortex velocity component in the transmitter direction for different radar beam locations for both the Taylor and the Oseen vortices, respectively. A narrow incident electromagnetic beam is used. In both Fig. 12 and Fig. 13, the solid line shows the exact velocity profile, and the results of the simulation are shown by circles. To generate Figs. 12 and 13, the

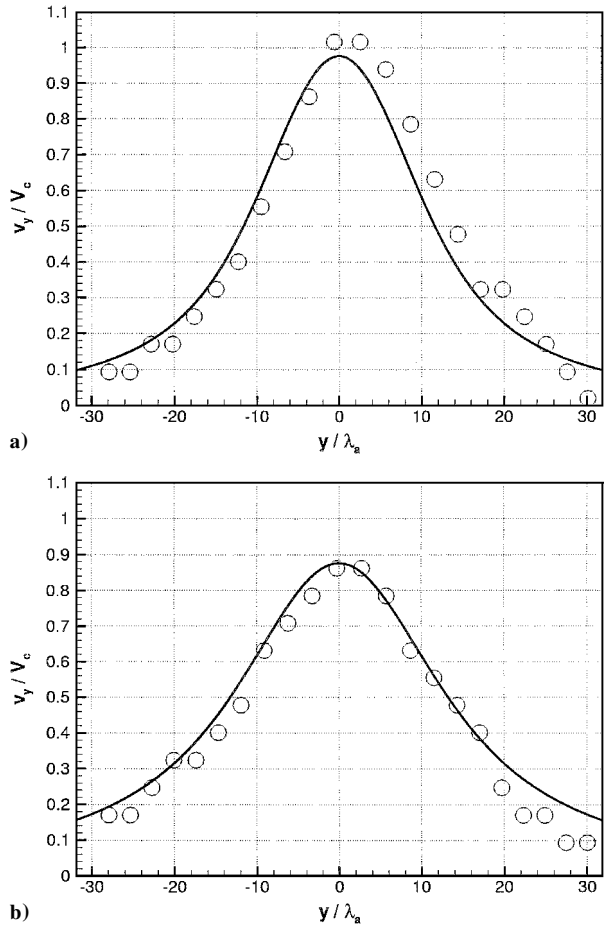

Fig. 13 Oseen vortex *y* component of the wake vortex velocity profiles: incident electromagnetic beam is a) $8\lambda_a$ and b) $14.3\lambda_a$ away from the vortex center in the *x* direction.

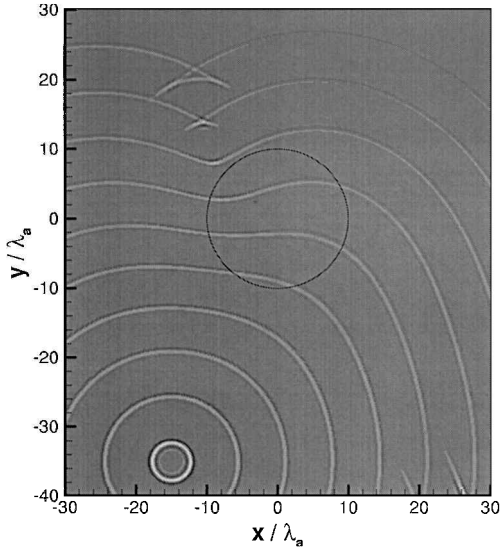

Fig. 14 Incident acoustic field at different times for a Taylor vortex; pulses from bottom to top correspond to $t = 20(2n - 1)/\omega_a$ s, $n = 1, 2, 3, \ldots, 10$, respectively.

backscattered electromagnetic signal is divided into a number of short time slices, and a spectral analysis is performed on each time slice.[18] Each slice consists of 150,000 samples and are zero padded to $2^{20} = 1{,}048{,}576$ samples. This gives a frequency resolution equal to 39.193 Hz, which corresponds to 6.532 m/s. It can be seen from Figs. 12 and 13 that the two-dimensional RASS simulation follows the exact velocity profile very well.

Figure 14 shows the incident acoustic field for the case where the acoustic source is located at $(-14.3\lambda_a, -35\lambda_a)$. A Taylor vortex with a core radius equal to $10\lambda_a$ is used. In this case, the velocity obtained from the spectral analysis of the backscattered signal should be negative because the wake vortex velocity is toward the receiver. Figure 15 shows the calculated vortex velocity component in the transmitter direction. The frequency resolution, time gating information, and zero padding in this case are similar to those in Figs. 12 and 13. Once again, it can be seen that the two-dimensional RASS simulation follows the exact velocity profile within the Fourier transform's resolution.

The results of the simulation become less accurate for large values of y/λ_a. The reasons may be explained as follows. Each circle in Figs. 12, 13, and 15 shows the vortex velocity averaged over a small area in the scatterer. The length of this area in the *y* direction depends

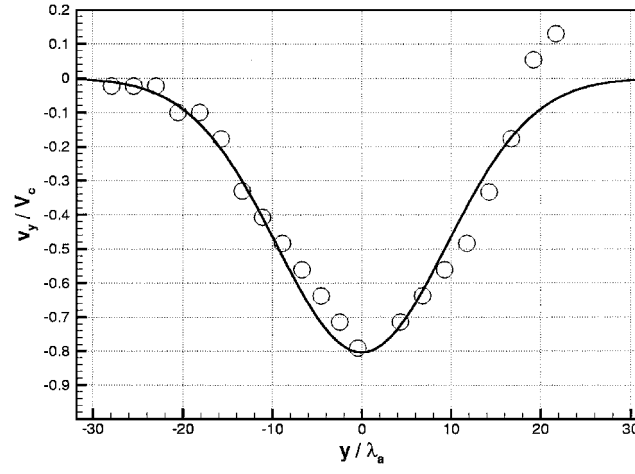

Fig. 15 Taylor vortex *y* component of the wake vortex velocity profiles incident electromagnetic beam is $-14.3\lambda_a$ away from the vortex center in the *x* direction: ——, exact and ○, numerical simulation.

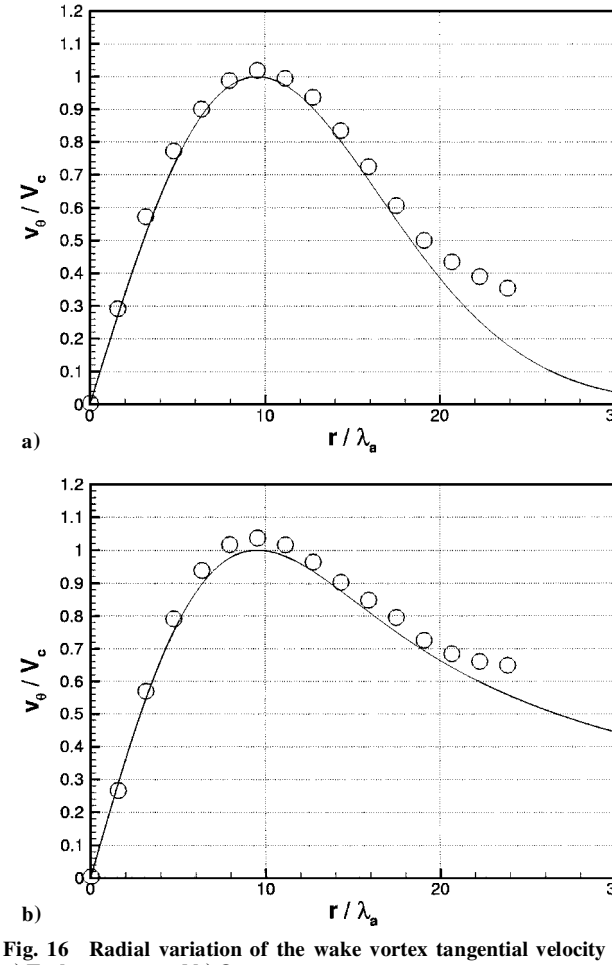

Fig. 16 Radial variation of the wake vortex tangential velocity for a) Taylor vortex and b) Oseen vortex.

on the time gate length, that is, the size of the time series slices. The width of this area in the x direction depends on the beam width at that particular location. For large values of y/λ_a, the beam width is larger and, therefore, the averaging is taken over a larger area, which results in a less accurate vortex velocity profile. Slight reflections from the boundary of the computational domain are also partially responsible for less accurate results close to the upper boundary.

The Abel transform may be applied to the results of the simulation at the different locations and the radial variation of the wake vortex velocity profile may be obtained. Figure 16 shows the results of the application of the Abel transform for the Taylor and Oseen vortices. The solid line shows the exact velocity profile and the circles show the results of the RASS simulation. As is clear from Fig. 16, the results of the RASS simulations are in very good agreement with the exact values, especially within the first two core radii.

C. Effect of the Beam Width

To investigate the effect of the incident electromagnetic beam width, the following numerical experiment is performed. A Taylor vortex with a core radius equal to $10\lambda_a$ and a core velocity equal to 85 m/s is considered. The transmitter and receiver antennas are located at $(15\lambda_a, -42\lambda_a)$ and $(15\lambda_a, -32\lambda_a)$, respectively. The acoustic source is located at $(15\lambda_a, -35\lambda_a)$. The transmitter antenna uses isotropic point source arrays in the broadside configuration. The beam width is then controlled by the number of point sources in the array.

Four different cases are considered. In these cases 161, 12, 6, and 3 sources are used to generate an HPBW equal to 0.7118, 9.5941, 19.4712, and 41.8103 deg, respectively. Figure 17 shows the y components of the wake vortex velocity profile associated with these cases. Figure 17a shows that, for a very narrow beam transmitter, the RASS simulation follows the exact velocity profile very accurately. As the transmitter beam width increases, the RASS measurements become less and less accurate. However, even for large beam widths, the RASS simulation still can predict the vortex velocity fairly accurately for locations close to the receiver. For a wide beam angle (Fig. 17d) the received signal includes information from a large area of the scatterer with both negative and positive Doppler shift. Therefore, the RASS results are scattered about zero mean flow velocity with a fairly high spread.

A very interesting result is obtained when a very wide beam angle is used. The electromagnetic transmitter and receiver are located at $(0, -42\lambda_a)$ and $(0, -32\lambda_a)$, respectively, and an isotropic point source array consisting of only two sources is used. The HPBW is then equal to 90 deg, and effectively the incident radar beam covers the entire computational domain. The acoustic source is located at $(0, -35\lambda_a)$. The computed velocities are shown in Fig. 18. In Fig. 18, R is the distance from the transmitter and V_R is the wake vortex velocity component in the transmitter direction. The circles are the velocity values obtained from the spectral analysis of the backscattered signal using the time gating technique. In addition, the solid line shows the exact values of the maximum wake vortex velocity at different distances from the receiver. A number of observations may be made. First, the velocity profile obtained from the RASS simulation using a wide radar beam is in fairly good agreement with the maximum wake vortex velocity at different distances from the receiver. Second, although both the negative and positive wake vortex velocities are in the radar beam of sight, the negative wake vortex velocities that give a positive Doppler shift give a stronger scattered signal. A negative velocity is obtained when the wake vortex velocity component is toward the receiver. This suggests that the signals coming from the regions that have a velocity component toward the receiver have a higher signal-to-noise ratio.

D. Two-Vortex Interaction

A wake vortex is generated at each aircraft wing tip. In the early stages of the evolution, these two vortices are separated by the aircraft wing span, and practically they have little effect on each other.

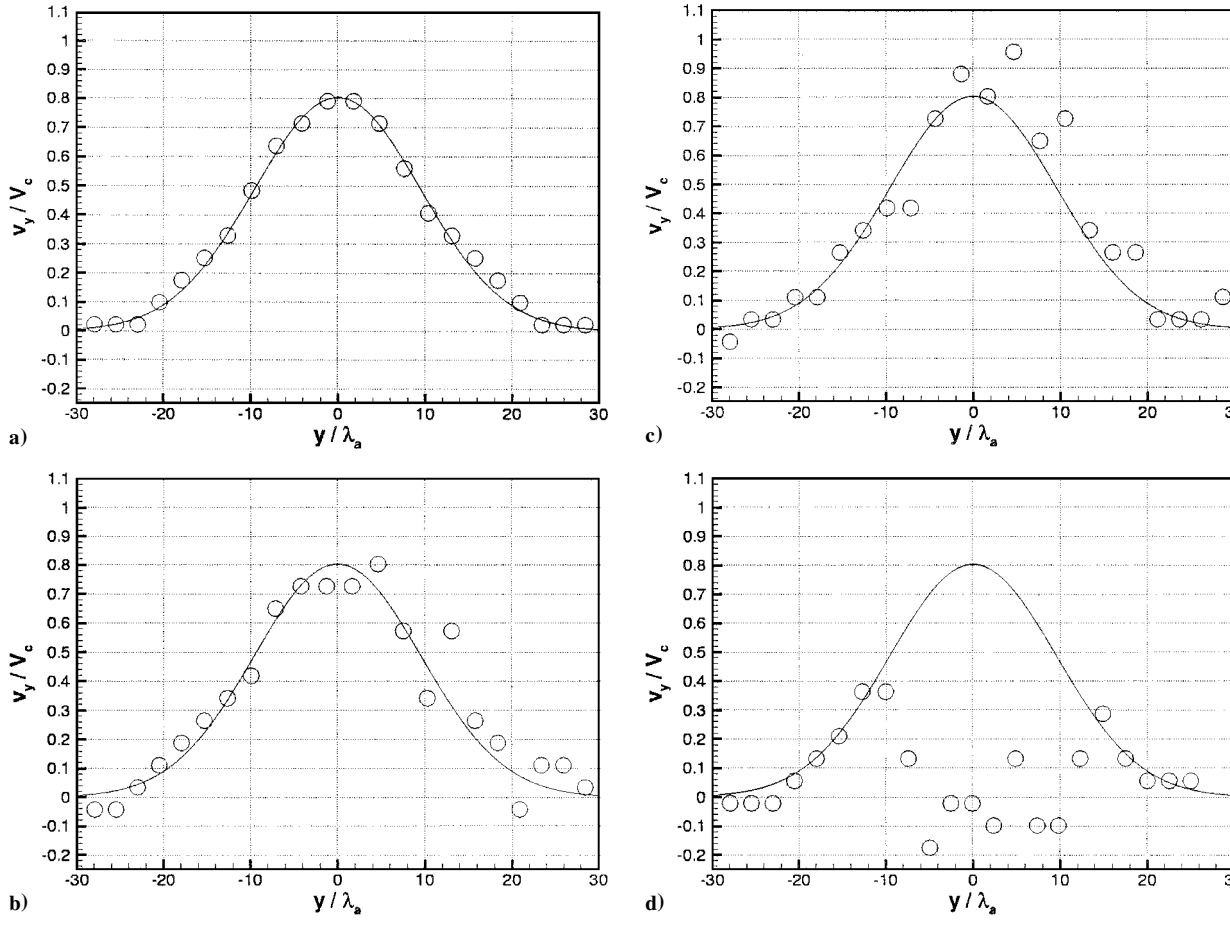

Fig. 17 Effect of beam width on the RASS measurements, y component of the wake vortex velocity profile for a Taylor vortex; incident electromagnetic beam is $15\lambda_a$ away from the vortex center in the x direction; ——, exact and ○, numerical simulation: HPBW = a) 0.7118 deg, b) 9.594 deg, c) 19.471 deg, and d) 41.810 deg.

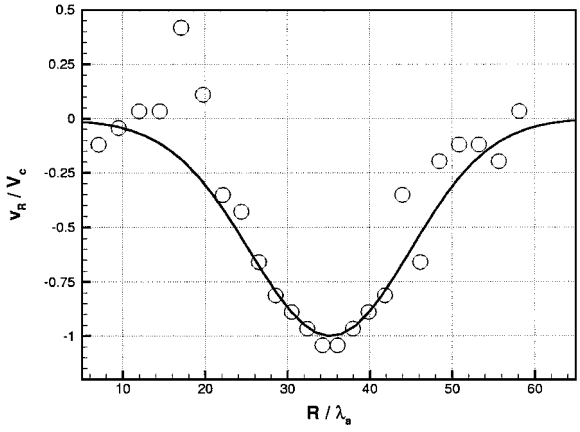

Fig. 18 Velocity profile obtained using a very wide radar beam width.

As time passes, they diffuse, and at some point they start to interact with each other. The mean flowfield is then a combination of their velocity profiles. A question that may be raised is whether the RASS simulation can detect them and reconstruct the associated flowfield. This section addresses issues regarding the two-vortex interactions.

In principle, the presence of two vortices makes no difference in the simulation. The code puts no restriction on the mean flow profile. In fact, the mean flowfield may be any arbitrary velocity profile. Therefore, the RASS simulation will successfully reconstruct the velocity profile along the incident electromagnetic field direction in a two-vortex case. However, the Abel transform may not be used in the two-vortex case. For the Abel transform to be valid, the mean flow has to be axisymmetric; a condition that is no longer met for two vortices.

The best approach to the simulation of the detection of two vortices is superposition. The governing differential equations are linear, and the Abel transform is also linear. Therefore, the simulation may be performed for each vortex separately, and the results may superimposed. In practice, however, it is not possible to consider each vortex at a time. It may then be necessary to use the Radon transform instead of the Abel transform. The Radon transform is the extension of the Abel transform for the case where the scatterer has no rotational symmetry.

V. Conclusions

In this paper, a two-dimensional simulation of aircraft wake vortex detection using RASS has been described. This has been achieved by sending an acoustic wave and a narrow radar beam and analyzing the spectrum of the scattered electromagnetic signal at a receiver antenna. The Doppler shift in the spectrum provides information that leads to a determination of the wake vortex velocity field within the accuracy of the spectrum resolution. To obtain results from the numerical simulations in a realistic computational time, the actual electromagnetic wave propagation speed has been replaced with a much lower value. This allows an explicit, time-accurate numerical scheme to be used. This approach has been shown to be valid in a previous study by the authors.[18]

A number of assumptions that had been made in the previous study have been improved. The one-dimensional Maxwell solver has been replaced by a two-dimensional simulation, the transmitter and receiver antennas have been modeled explicitly in the numerical simulation, and the effect of radar beam width has been shown. Both a short, single-frequency acoustic pulse and a continuous broadband acoustic source have been considered, and both monostatic and bistatic configurations have been studied. However, a number of other issues still remain to be considered, including the effects of atmospheric turbulence, the time evolution of the wake vortex, and the three-dimensional nature of wake vortices.

The use of RASS for wake vortex detection offers considerable promise as an alternative wake vortex sensing system. The present study shows clearly that the RASS is a viable instrument that can provide a great deal of information about wake vortices behind aircraft in the vicinity of airports.

References

[1]Smith, P. L., "Remote Measurement of Wind Velocity by the Electromagnetic-Acoustic Probe, I: System Analysis," *Proceedings of the 5th National Convention Military Electronics*, 1961, pp. 48–53.

[2]Fetter, R. W., "Remote Measurement of Wind Velocity by the Electromagnetic-Acoustic Probe, II: Experimental System," *Proceedings of the 5th National Convention Military Electronics*, 1961, pp. 54–59.

[3]Marshall, J. M., Peterson, A. M., and Barnes, A. A., Jr., "Combined Radar–Acoustic Sounding System," *Applied Optics*, Vol. 11, No. 7, 1972, pp. 108–112.

[4]North, E. M., Peterson, A. M., and Parry, H. D., "RASS, A Remote Sensing System for Measuring Low-Level Temperature Profile," *Bulletin of the American Meteorological Society*, Vol. 54, No. 9, 1973, pp. 912–919.

[5]Tsuda, T., Masuda, Y., Inuki, H., Takahashi, K., Takami, T., Sato, T., Kato, S., and Fukao, S., "High Time Resolution Monitoring of Tropospheric Temperature with a Radio Acoustic Sounding System (RASS)," *Pure and Applied Geophysics*, Vol. 130, No. 2/3, 1989, pp. 497–507.

[6]May, P. T., Strauch, R. G., Moran, K. P., and Ecklund, W. L., "Temperature Sounding by RASS with Wind Profiler Radar: A Preliminary Study," *IEEE Transactions on Geoscience and Remote Sensing*, Vol. 28, No. 1, 1990, pp. 19–28.

[7]Ecklund, W. L., Carter, D. A., Balseley, B. B., Currier, P. E., Green, J. L., Weber, B. L., and Gage, K. S., "Field Tests of a Lower Tropospheric Wind Profiler," *Radio Science*, Vol. 25, No. 5, 1990, pp. 899–906.

[8]Matuura, N., Masuda, Y., Inuki, H., Sato, T., Kato, S., Fukao, S., and Tsuda, T., "Radio Acoustic Measurement of Temperature Profile in the Troposphere and Stratosphere," *Nature*, Vol. 323, No. 2, 1986, pp. 426–428.

[9]Peters, G., Hinzpeter, H., and Baumann, G., "Measurements of Heat Flux in the Atmospheric Boundary Layer by Sodar and RASS: A First Attempt," *Radio Science*, Vol. 20, No. 6, 1985, pp. 1555–1564.

[10]Tatarski, V. I., *Wave Propagation in a Turbulent Medium*, McGraw–Hill, New York, 1961, pp. 59–80.

[11]Nalbandyan, O. G., "Scattering of Electromagnetic Waves from a Sound Wave Propagating in a Turbulent Atmosphere," *Izvestiya, Academy of Sciences, USSR, Atmospheric and Oceanic Physics*, Vol. 12, No. 8, 1976, pp. 877–880 (English translation).

[12]Kon, A. I., "Signal Power in Radioacoustic Sounding of a Turbulent Atmosphere," *Izvestiya, Academy of Sciences, USSR, Atmospheric and Oceanic Physics*, Vol. 20, No. 2, 1984, pp. 131–135 (English translation).

[13]Kon, A. I., "Combined Effect of Turbulence and Wind on the Signal Intensity in Radioacoustic Sounding of the Atmosphere," *Izvestiya, Academy of Sciences, USSR, Atmospheric and Oceanic Physics*, Vol. 21, No. 12, 1984, pp. 942–947 (English translation).

[14]Bhatnagar, N., and Peterson, A. M., "Interaction of Electromagnetic and Acoustic Waves in a Stochastic Atmosphere," *IEEE Transactions on Antennas and Propagation*, Vol. AP-27, No. 3, 1979, pp. 385–393.

[15]"Measurement of Atmospheric Parameters with a Bistatic Radar Supplemented by an Acoustic Source," Environmental Surveillance Technology Programme, Oslo, Oct. 1995.

[16]"Estimation of Wind Turbulence and Wake Vortexes by Scatter Propagation Methods Involving Radio and Acoustic Waves," Environmental Surveillance Technology Programme, Oslo, Oct. 1995.

[17]Rubin, L. W., Burnham, D. C., Spitzer, E. A., and Rudis, R. P., "A Robust Low Cost Airport Wake Vortex Sensor," AIAA Paper 2000-0627, 2000.

[18]Boluriaan, S., and Morris, P. J., "Numerical Simulation of Wake Vortex Detection Using a Radio Acoustic Sounding System," *AIAA Journal*, Vol. 39, No. 6, 2001, pp. 1097–1105.

[19]Kraus, J. D., and Carver, K. R., *Electromagnetics*, McGraw–Hill, New York, 1973, pp. 601–715.

[20]Nestor, O. H., and Olsen, H. N., "Numerical Method for Reducing Line and Surface Probe Data," *SIAM Review*, Vol. 2, No. 3, 1960, pp. 200–207.

[21]Neufville, A. D., "The Dying Vortex," *Proceeding Fifth Midwestern Conference on Fluid Mechanics*, Univ. of Michigan, Ann Arbor, MI, 1957, p. 365.

[22]Taylor, G. I., "On the Dissipation of Eddies," *The Scientific Papers of Sir Geoffrey Ingram Taylor*, Vol. 2, edited by G. K. Batchelor, Cambridge Univ. Press, Cambridge, England, U.K., 1960, pp. 96–101.

[23]Panton, R. L., *Incompressible Flow*, Wiley, New York, 1984, pp. 283–288.

[24]Tam, C. K. W., and Webb, J. C., "Dispersion-Relation-Preserving Difference Schemes for Computational Aeroacoustics," *Journal of Computational Physics*, Vol. 107, No. 2, 1993, pp. 262–281.

[25]Boluriaan, S., "Parallel Direct Numerical Simulation of Wake Vortex Detection Using Monostatic and Bistatic Radio Acoustic Sounding Systems," Ph.D. Dissertation, Dept. of Aerospace Engineering, Pennsylvania State Univ., University Park, PA, Aug. 2000.

[26]Bayliss, A., and Turkel, E., "Radiation Boundary Conditions for Wave-Like Equations," *Communications on Pure and Applied Mathematics*, Vol. 33, 1980, pp. 707–725.

H. M. Atassi
Associate Editor